Self-organization optomagnetic $CoFe_2O_4$/ZnS nanocomposite: preparation and characterization

Ali Amiri Zarandi [a,b], *Ali A. Sabbagh Alvani* [b,*], *Reza Salimi* [b], *Hassan Sameie* [b]

Shima Moosakhani [a,b], *Dirk Poelman* [c], *Federico Rosei* [d,e]

[a] Faculty of Polymer Engineering & Color Technology, Amirkabir University of Technology (Tehran Polytechnic), Tehran, Iran

[b] Color and Polymer Research Center (CPRC), Amirkabir University of Technology (Tehran Polytechnic), Tehran, Iran

[c] LumiLab, Department of Solid State Sciences, Ghent University, Belgium

[d] INRS Centre for Energy, Materials and Telecommunications, 1650 Boul. Lionel Boulet, J3X 1S2 Varennes (QC) Canada

[e] Department of Chemistry and Center for Self-Assembled Chemical Structures, McGill University, 801 Sherbrooke Street West, Montréal, QC H3A 2K6, Canada

*Corresponding author: sabbagh_alvani@aut.ac.ir

Tel: (+98-21) 66418600

FAX: (+98-21) 66418601

Abstract

We report an advanced method for the self-organization of an optomagnetic nanocomposite composed of both fluorescent clusters (ZnS quantum dots, QDs) and magnetic nanoparticles ($CoFe_2O_4$). ZnS nanocrystals were prepared via an aqueous method at different temperatures (25, 50, 75, and 100 °C). Their structural, optical and chemical properties were comprehensively characterized by X-ray diffraction (XRD), UV-Vis, photoluminescence (PL) spectroscopy, scanning electron microscopy (SEM), dynamic light scattering (DLS), transmission electron microscopy (TEM), and infrared spectroscopy (FT-IR). The highest PL intensity was observed for the cubic ZnS nanoparticles synthesized at 75 °C which were then stabilized electrosterically using thioglycolic acid. The photophysical analysis of the capped QDs with particle size in the range 9-25 nm revealed that the emission intensity increases and the optical band gap rises compared to uncapped nanocrystals (3.88 to 4.02 eV). These band gaps are both wider than that of bulk ZnS resulting from the quantum confinement effect. Magnetic nanoparticles were synthesized via a co-precipitation route and a sol-gel process was used to form the functionalized, silica-coated $CoFe_2O_4$. Finally, thiol coordination was used for binding the QDs to the surface of the magnetic nanoparticles. The fluorescence intensity and magnetic properties of the nanocomposites are related to the ratio of ZnS and $CoFe_2O_4$. As-prepared optomagnetic nanocomposite with small size (12-45 nm), acceptable saturation magnetization (about 6.7 emu/g), and satisfactory luminescent characteristics could be successfully prepared. These are promising candidates for biological and photocatalytic applications.

Keywords: Optomagnetic, Quantum dots, Magnetic nanoparticles, Multifunctional Nanocomposite

1. Introduction

During the past two decades, nanostructured materials have shown to be of special interest because of their fundamental new properties and for their potential use in a broad range of applications [1-6]. In particular, optomagnetic nanocomposites have attracted attention in recent years due to their multifunctional properties, thereby expanding their use in photocatalyis and biomedical application such as multimodal fluorescence imaging, magnetic resonance imaging (MRI), magnetic separation and drug targeting [7-9]. More specifically, magnetic nanoparticles (MNPs) combined with QDs have been developed into specific functionalized luminescent magnetic nanocomposites (LMNs), which have the advantages of both MNPs and QDs [10-12]. In this case, MNPs can be manipulated under an external magnetic field and the QDs can serve as luminescent markers [13].

Several groups have investigated the optical and magnetic properties of optomagnetic nanocomposites. He et al. used lanthanide doped nanoparticles to prepare Fe_3O_4@LaF_3:CeTb magnetic-optical nanoparticles [14]. Shen et al. succeeded in achieving insulin delivery, cell imaging, and antidiabetic research of dietary supplements by using chitosan [15]. Liu et al. used a sonochemical route to prepare Fe_3O_4@CdS nanocomposites which can be used as photocatalysts in practical applications [16]. However, because of the lattice nonconformity of the components, it is difficult for QDs to directly coat magnetic particles. To address these challenges, some intermediate layers such as amorphous silica can be used as spacers in the synthesis of nanocomposites [17-19].

In recent years, QDs have been studied extensively due to their novel photophysical properties and potential use in applications such as biomolecular recognition, lasers, and photovoltaic devices [20-24]. Some of the most interesting properties of these advanced nanomaterials are broad optical

excitation, tunable and narrow emission spectrum, excellent photo stability, and size-dependent physic-chemical properties. Such properties are affected by two main factors: drastic changes in surface to volume ratio and electronic structure of the precursors [25-27].

Zinc sulfide (group II-VI semiconductor, direct wide band gap) nanoparticles have recently attracted significant attention because of their applications in biology and optoelectronic devices [28-32]. In general, the synthesis temperature has a significant effect on the crystal growth, structure and optical properties of the QDs. These studies suggest that the ideal growth temperature should be high enough to overcome the energy barrier for nucleation and growth, and low enough to result in a surface reconstruction leading to optimization of properties [33].

It is also noteworthy that with a suitable surface modification using organic ligands such as non-toxic mercaptans allows to obtain ZnS nanoparticles which exhibit enhanced luminescence properties, water-solubility, colloidal stability, and size controllability [34-36].

On the other hand, MNPs have been extensively studied due to their wide applications, such as biomedicine and bioimaging [37,38]. Among superparamagnetic metal oxide nanoparticles, Ferrites including $M_{1-x}Zn_xFe_2O_4$ and $Fe_{1-x}M_xFe_2O_4$ (M=Co, Mn) would be superior for various applications, yet must be stabilized by attachment of organic and organic-inorganic molecules on the surface of the particles [39,40]. Cobalt ferrite ($CoFe_2O_4$) is one of the most important spinel ferrites, which has been widely studied due to its moderate saturation magnetization, large anisotropy and chemical stability [41].

In this paper, firstly, we use a wide range of synthesis temperatures in an effort to understand its influence on the crystallite size and optical properties of ZnS QDs. Secondly, we investigate the effect of thioglycolic acid as capping agent on the luminescence characteristics of the

nanoparticles. Finally, we report an inexpensive, green, and efficient method for the preparation of $CoFe_2O_4$/ZnS nanocomposites under ambient condition via an aqueous method by using silica as transition layer.

2. Experimental section

2.1. Materials

Tetraethylorthosilicate (TEOS), thioglycolic acid (TGA), 3-mercatopropyl-trimethoxysilane (MPS), ammonia (25 wt %), and absolute ethanol (99.7%) were purchased from Merck. Extra pure Iron(III) chloride hexahydrate, Cobalt(II) chloride hexahydrate, sodium hydroxide, tri-Sodium citrate dihydrate, zinc acetate, and sodium sulfide were all purchased from Scharlau. All reagents were analytical grade and used without further purifications. Double distilled water was used in all experiments.

2.2. Synthesis of capped and uncapped ZnS QDs

ZnS QDs were synthesized using a wet chemical method, in an aqueous medium under air atmosphere. Aqueous solutions of zinc acetate (0.4M) and Na_2S (0.4M) were distinctly prepared. Na_2S was added drop-wise to zinc acetate under stirring at room temperature. Next, various synthesis temperatures (25, 50, 75, 100 °C) were applied and stirring was continued for 30 min. The collected precipitates were washed three times using de-ionized water by centrifuging at 8000 rpm for 8 min to remove unreacted reagent and impurities. Finally, the washed particles were dried at 60 °C in air for 12h.

To control the particle size and colloidal stability, repulsive forces must be added between the nanoparticles to inhibit agglomeration and aggregation. In this regard, capped ZnS QDs were synthesized according to the same steps mentioned above with adding TGA dropwise before the addition of Na_2S, which leads to arrest the agglomerating by stabilizing QDs electrostatically. (Scheme 1a) [42].

2.3. Synthesis of $CoFe_2O_4$ magnetic nanoparticles

The $CoFe_2O_4$ MNPs were synthesized by a co-precipitation technique based on the hydrolysis of Co^{2+} and Fe^{3+} salts in the molar ratio of 1:2 [43]. Cobalt ferrite has an inverse spinel structure where oxygen atoms are located in an fcc lattice, one half of the Co^{2+} ions occupy the octahedral sites and the other half, together with Fe^{3+} ions are located at tetrahedral positions [44].

Aqueous solutions of $CoCl_2.6H_2O$ (0.2M) and $FeCl_3.6H_2O$ (0.4M) were prepared. The cobalt(II) chloride precursor was added to the iron chloride under continuous stirring and nitrogen protection at room temperature. Next, a solution of 3.0 M NaOH was added dropwise to the Co^{2+}/Fe^{3+} mixture, under vigorous stirring. The color of solution changed immediately to orange, which indicated that the precipitation had occurred and $Fe(OH)_3$ was formed. The pH of the solution was permanently monitored and sodium hydroxide was progressively added to adjust the pH of aqueous dispersion to 11–12. Then, the temperature was raised to 70 °C and stirring was continued for 30 min. To remove unreacted reagent and impurities, the particles were washed as mentioned until the pH level was reduced from approximately 12 to 7 – 8.

It is important to keep the molar ratio of Fe^{3+}/Co^{2+} at 2:1, to obtain pure magnetic nanoparticles. If the molar ratio is less than 2, the as-prepared products are unstable and oxidize in air while above 2, Fe_2O_3 impurities exist in the final product [45].

2.4. Synthesis of magnetic/fluorescent nanocomposites

To incorporate the MNPs with QDs, a silica shell was coated onto the magnetic particles by a sol–gel process to construct the $CoFe_2O_4@SiO_2$ structure. In a typical procedure, 0.2 g $CoFe_2O_4$ nanoparticles were first diluted with a solution of Tri-sodium citrate (0.5M). Under ultrasonic irradiation for 30 min, MNPs coordinated with citric acid ions and their dispersibility improved. Subsequently, the resulting products were washed and redispersed in distilled water after weighing. The obtained magnetic liquid was coated with amorphous silica through the hydrolysis of a sol–gel precursor. For this purpose, the ferrofluid was added to a mixture of distilled water, absolute ethanol, and ammonia solution in the volume ratio of 10:6:0.5. Next, 21 microliters of TEOS were dissolved in absolute ethanol and added to the solution above. The reaction was allowed to proceed at 37 °C for 8 h under continuous stirring. Then, in order to form the functional $CoFe_2O_4@SiO_2$-SH structure, the second sol–gel process was performed as follows: 92 microliters of MPS were dissolved in absolute ethanol and added to a freshly prepared $CoFe_2O_4@SiO_2$ solution under vigorous stirring. This hydrolysis reaction proceeded for 12 h at 37 °C. At this stage, the functional nanoparticles could be used to combine with TGA-capped ZnS QDs through the thiol coordination. For this purpose, the solution of luminescent nanoparticles was quickly added to the functional MNPs solution and the two were kept under stirring at 37 °C for 6 h. Some of the obtained particles could be separated with magnetic harvesting from the solution. These were then

washed using de-ionized water by centrifuging at 6000 rpm for 6 min. Finally, the washed particles were dried at 60 °C in air for 12h. All synthesized samples are described in Table 1.

Table 1. Molar ratio of precursors for different samples

Sample	Temperature	Zn:S	TGA:Zn	QDs:MNPs
ZnS25	25 °C	1:1	Without TGA	Without MNPs
ZnS50	50 °C	1:1	Without TGA	Without MNPs
ZnS75	75 °C	1:1	Without TGA	Without MNPs
ZnS100	100 °C	1:1	Without TGA	Without MNPs
TGA-ZnS	75 °C	1:1	1:1	Without MNPs
LMN1:1	37 °C	1:1	1:1	1:1
LMN4:1	37 °C	1:1	1:1	4:1
LMN8:1	37 °C	1:1	1:1	8:1
LMN16:1	37 °C	1:1	1:1	16:1
LMN32:1	37 °C	1:1	1:1	32:1

Scheme 1b shows the general procedure of TEOS adsorbing on the surface of magnetic nanoparticles. The solution of TEOS is added to the ferrofluid and reacted with H_2O on the surface of $CoFe_2O_4$ to connect Si-O with nanoparticles. Latter, hydrolysis of TEOS brings $-OCH_2CH_2$ groups to transfer into -OH groups. Further, the neighbor -OH group loses a molecule of H_2O to form a cross-linked structure and hence the SiO_2 coating is formed [46,47]

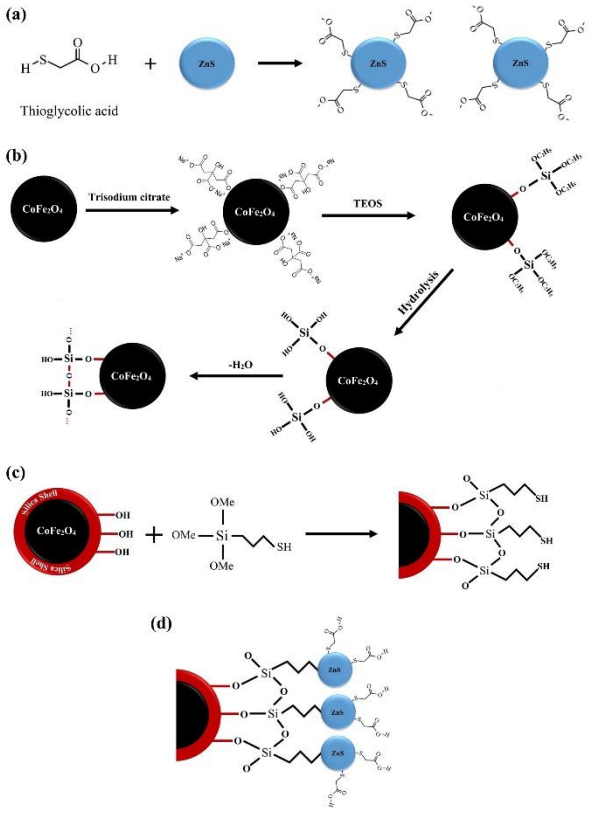

Scheme 1. Schematic procedure of TGA (a) and TEOS (b) adsorbing on the surface of nanoparticles, functionalizing strategy for MNPs (c), assembly of LMNs (d)

Scheme 1c illustrates the functionalization strategy for magnetic nanoparticles. The silanes are selected in such a way that silica shell formation is initiated at the surface of the NPs. MPS can be directly polymerized on the surface of $CoFe_2O_4$-core/silica-shell under basic conditions because NPs have a dominant hydroxide-terminated surface and thus silane hydrolysis and polymerization initiate from the surface of the nanoparticles [48].

As evident in scheme 1d, at the last step of the assembly procedure, the thiol coordination is used to bind TGA-capped QDs to the surface of the MNPs. In addition, there are lots of functional carboxylic groups outside the nanocomposites that could further react with some ligands or modified polymers. The advantage of the method used herein is the tunable saturation magnetization (M_s) and luminescence behavior of the final nanocomposites that were assembled with the magnetic nanoparticles and QDs. Such multifunctional nanostructures may realize multiseparations by using a tunable magnetic field in just one process [49]. We therefore expect that this method for assembling nanostructures may be useful to widen the applications of LMNs.

2.5. Measurement and characterization

UV-Vis and PL spectra were measured using a JENWAY 6715 UV-Vis and Perkin-Elmer LS-55 fluorescence spectrophotometer, respectively. TEM images were acquired with a JEOL 2010 transmission electron microscope after placing the particle solution on a carbon-coated copper grid followed by drying the sample. Fourier transform infrared spectra were recorded with a Perkin Elmer FT-IR Spectrum 100 to investigate the presence of the organic ligands. DLS study and zeta potential measurement was performed using Malvern Zeta sizer Nano S. The structure of QDs and LMNs were also investigated under a Stereoscan S 360 SEM. Finally, magnetic measurements

were performed using a vibrating sample magnetometer (VSM) with a maximum applied field of 1100 kA/m.

3. Results and discussion

3.1. QDs characterization

3.1.1. Effect of synthesis temperature

XRD patterns of ZnS powders synthesized at different temperatures are displayed in Fig. 1a. The three main diffraction peaks at 2θ values of 29.2°, 48.5° and 56.9° correspond to (111), (220), and (311) lattice lanes, respectively, which match well with those of cubic ZnS (JCPDS card no. 80-0020). Figure 1a also shows that the crystallinity of particles improves as the temperature is increased.

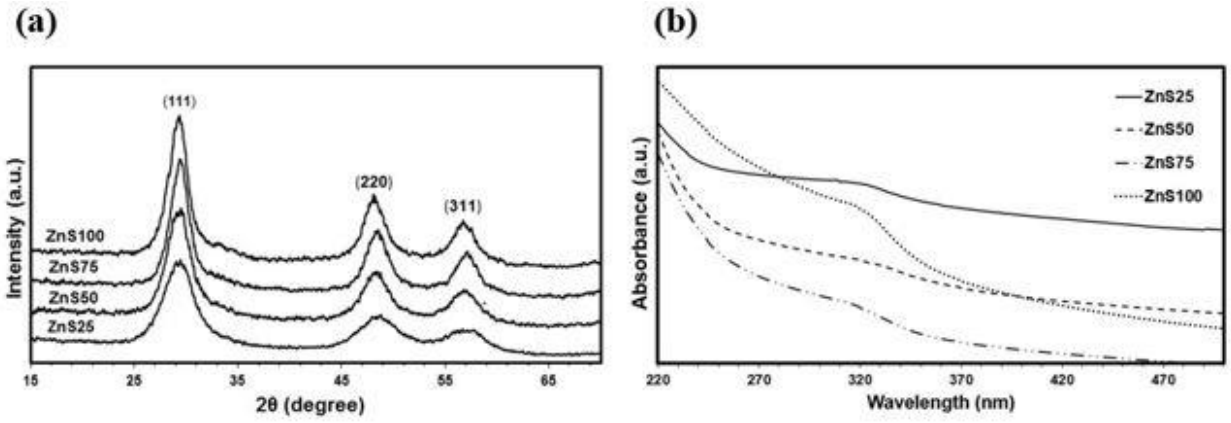

Figure 1. XRD patterns (a) and UV-visible absorption spectra (b) of ZnS nanocrystals synthesized at different temperatures

The broadening of XRD peaks in Fig. 1a demonstrates that particle sizes of all samples are in the nanometer range. The average crystallite size can be estimated from the half-width of the diffraction peaks by using the Debye–Scherrer's equation [50]:

$$D = \frac{k\lambda}{\beta \cos\theta} \quad (1)$$

where D is the average crystallite size, k is a geometric factor (equal to 0.89), λ is the wavelength of monochromatic X-rays (equal to 1.5404 Å for the CuKα radiation used), β is the full-width at half maximum of the diffraction peak, and θ is the diffraction angle. The average crystallite sizes of the ZnS25, ZnS50, ZnS75, and ZnS100 nanoparticles are found to be 2.9, 3.5, 4, and 4.3 nm, respectively. Thus, the average crystallite size increases with an increase in synthesis temperature, allowing therefore to control the size of the crystallites. The growth process is based on Ostwald ripening which suggests that crystallite size increases with increase in reaction temperature because when the free atoms in solution are supersaturated, they will tend to condense on the surface of larger particles. Consequently, the minor particles shrink, while the larger particles grow [51,52].

UV-Visible spectral analysis is a technique for characterization of semiconductor nanoparticles by which the quantum size effect could be derived from the position of the absorption edge. The spectra of ZnS25, ZnS50, ZnS75, and ZnS100 in Fig. 1b exhibit an absorption band edge at 317 nm (3.91 eV), 318 nm (3.89 eV), 319 nm (3.88 eV), and 321 nm (3.86 eV), respectively. It is significant, because it reveals a substantial blue shift of the absorption from that of 338 nm (3.66 eV) for bulk ZnS crystals at room temperature [53]. Since the crystallite size of prepared ZnS nanoparticles is nearly similar to the Bohr radius of excitons in bulk ZnS, the quantum confinement effect is expected to occur within these samples. Specifically, we observed that the band-gap energy slightly shifts to a higher wavelength when increasing the synthesis temperature.

The variation of band-gap can be used for estimating the crystallite radius (r) using the effective mass approximation by the Brus equation [54], given by:

$$\Delta E = E(r) - E(bulk) = \frac{h^2\pi^2}{2r^2}\left(\frac{1}{m_e^*} + \frac{1}{m_h^*}\right) - \frac{1.8e^2}{4\pi\varepsilon\varepsilon_0 r} + S(r) \quad (2)$$

where $E(r)$ is the band-gap of the nanoparticles, $E(bulk)$ is the band-gap of bulk ZnS, m_e^* and m_h^* are the effective masses of electron and hole in ZnS, respectively ($m_e^* = 0.34m_0$ and $m_h^* = 0.23m_0$, where $m_0 = 9.11\times10^{-31}kg$ is the free-electron mass) [55]. For all synthesis temperatures, the crystallite size of samples is estimated to be 3-4 nm, in reasonable agreement with the results of XRD analysis. Optical absorbance properties and crystallite sizes of ZnS nanoparticles estimated from XRD patterns and Brus equation are summarized in Table 2.

Table 2. Comparison of optical absorption edge and mean size of nanocrystals

Sample	Band edge (nm)	Band edge (eV)	Crystallite size from XRD (nm)	Crystallite size from EMA (nm)
ZnS25	317	3.91	2.9	3.39
ZnS50	318	3.89	3.5	3.53
ZnS75	319	3.88	4	3.63
ZnS100	321	3.86	4.3	3.81

In order to find the optimal synthesis temperature yielding the highest PL intensity, this parameter was changed from 25 to 100 °C. Figure 2a and its inset depict the room-temperature PL spectra of samples under excitation of 397 nm and the PL intensities plotted as a function of the synthesis temperature, respectively.

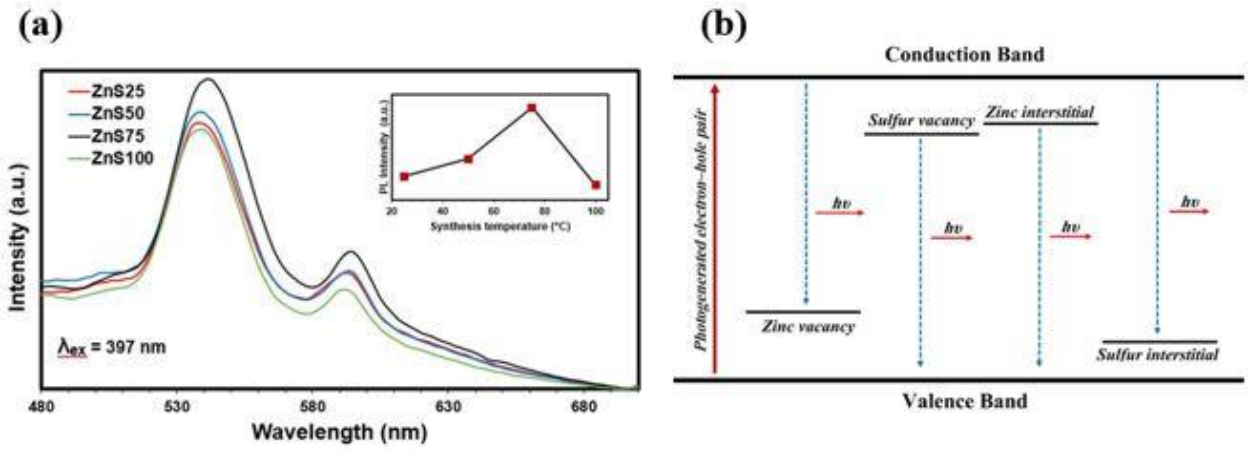

Figure 2. PL spectra and the PL relative intensities (inset) of ZnS syhthesized at different temperatures (a), Schematic energy level diagram for the defects in ZnS nanocrystals (b)

The surface state plays a significant role in determining the luminescence characteristics of the QDs [56]. Although the Schottky and Frenkel defects are the most important ones that exist in all solids, there is a tendency for only one type of them to be dominant since their formation energies are unequal [57]. The Frenkel defects are formed by dislocating ions in the crystal structure, thereby creating point defects in ZnS particles, which always serve as luminescent sites during PL processes. Zinc vacancies and interstitial sulfur atoms are equivalent to localized acceptor states while sulfur vacancies and interstitial zinc atoms lead to donor states (Fig. 2b). As the zinc ions are smaller than the sulfur ions, interstitial sulfur atoms causes more strain to the lattice. Because of such strain, electron levels originating from this site would have smaller binding energies. Therefore, the interstitial zinc states should be located far more to the conduction band edge than

the interstitial sulfur state to the valence band edge. In the same way, the levels associated with the zinc vacancies should be located far more to the valence band edge than those of sulfur vacancies to the conduction band edge [58]. As evident from Fig. 2a, the main emission peaks are at about 538 nm and 595 nm, which are ascribed to existence of interstitial zinc state and vacancy defects, respectively [59].

The most remarkable feature of Fig. 2a is the enhancement of PL intensities when the synthesis temperature was increased to 75 °C and decrease with further increasing temperature. The relatively lower PL intensities for the ZnS25 and ZnS50 than ZnS75 are attributed to the relationship between particle size and surface area. When the particle size becomes too small, the surface area increases, and this leads to a large number of dangling bonds and consequently non-radiative defects present on the surface of fine particles [60]. On the other hand, if the synthesis temperature is very high, the luminescent properties decline due to the large particle size because of the strong localization possible in nano-sized powders [61-62].

The variation of emission color with synthesis temperature is presented in a CIE chromaticity diagram, as shown in Fig. 3. The chromaticities of all emissions fall within a restricted area on the center of the diagram. As can be observed, the color unsaturation of ZnS75 emission (x=0.47, y=0.3) is less than ZnS25 (x=0.29, y=0.44), ZnS50 (x=0.28, y=0.45), and ZnS100 (x=0.27, y=0.46).

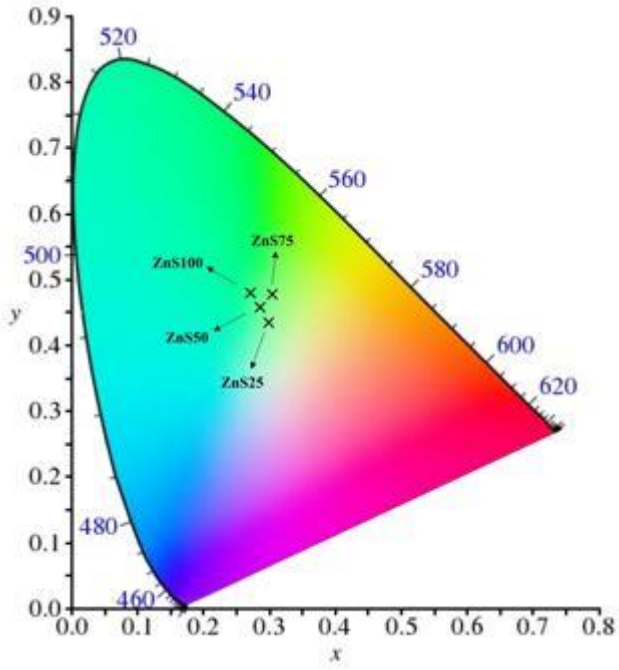

Figure 3. The emission chromaticities of ZnS nanoparticles

3.1.2 Effect of capping agent

To obtain colloidal stability and high fluorescence intensity of QDs, the use of capping ligands is an important method. The optimum synthesis temperature yielding the highest PL intensity was found to be 75 °C. Therefore ZnS75 was used as the standard sample and TGA was used as capping agent for further investigations.

Figure 4 illustrates the FT-IR spectra of uncapped and TGA-capped ZnS nanoparticles. The broad peaks at 2800-3700 cm^{-1}, 1635-1640 cm^{-1} correspond to the -OH and C=O stretching, respectively. The peaks at 1110 cm^{-1} and 1147 cm^{-1} in the TGA-ZnS sample are mainly due to C-O stretching, which signifies that the carboxylic acid groups remain on the surface of the ZnS nanoparticles. The peak at 1400 cm^{-1} due to C–S bonds was also detected from the FT-IR spectra. Finally, the peak at 665 cm^{-1} is related to Zn-S and S-S bond in the samples. S-H bond stretching,

which occurred at 2565 cm^{-1} in spectra of the TGA, relates to sulfhydryl (-SH) that vanishes in TGA-ZnS sample, which indicates that capping ligands have bounded with Zn atoms and form a complex. These results represent that TGA molecules have successfully capped the ZnS as stabilizer through the formation of a covalent bonds [63,64].

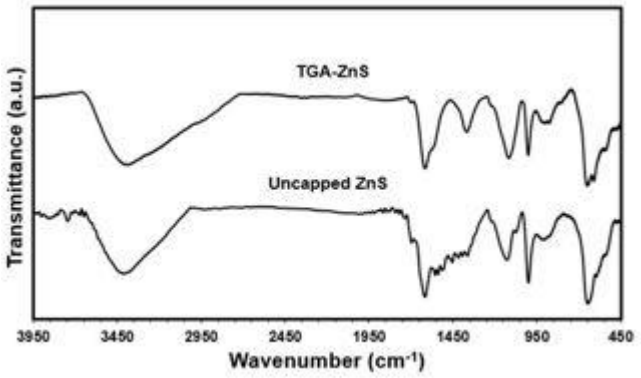

Figure 4. FT-IR spectra of capped and uncapped ZnS QDs

The SEM images (Fig. 5) of the ZnS samples possess aggregated grains consist of spherical shaped particles with a size distribution in the range of 25-125 and 9-25 nm for ZnS75 and TGA-ZnS, respectively.

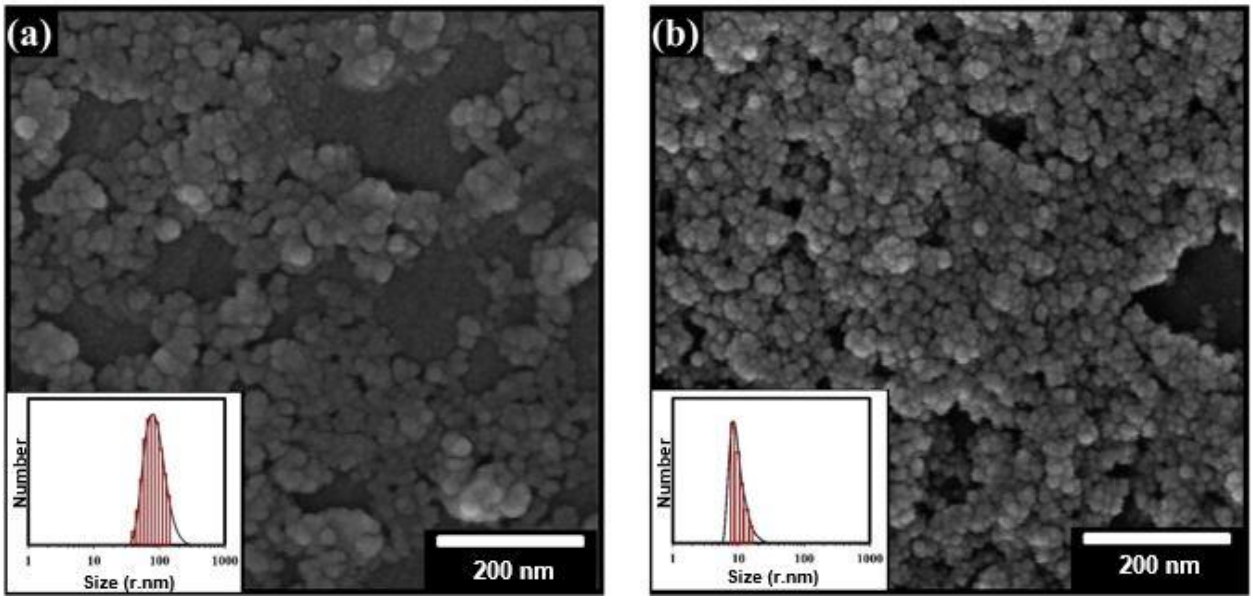

Figure 5. SEM micrographs and DLS curves (inset) of ZnS75 (a) TGA-ZnS (b) nanocrystals

The inset of Fig. 5 represents the DLS measurements for ZnS75 in the presence and absence of TGA. Both DLS and SEM confirm the presence of nanosized particles. The particle size of ZnS75 is in the range of 52-147 nm, while for TGA-ZnS the value is significantly smaller (8-22 nm). Generally, the DLS results and SEM observations indicate that the Particle radius shrinks remarkably in the presence of TGA.

The TEM image of TGA-ZnS with a size distribution around 2.5–4 nm are shown in Fig. 6. This range of value is in good agreement with the size estimated from the Brus relation. Moreover, the zeta potential for both ZnS75 and TGA-ZnS samples was measured as -19.9 and -31.5 mV, respectively, which clarifies using a capping agent significantly improves the colloidal stability of QDs.

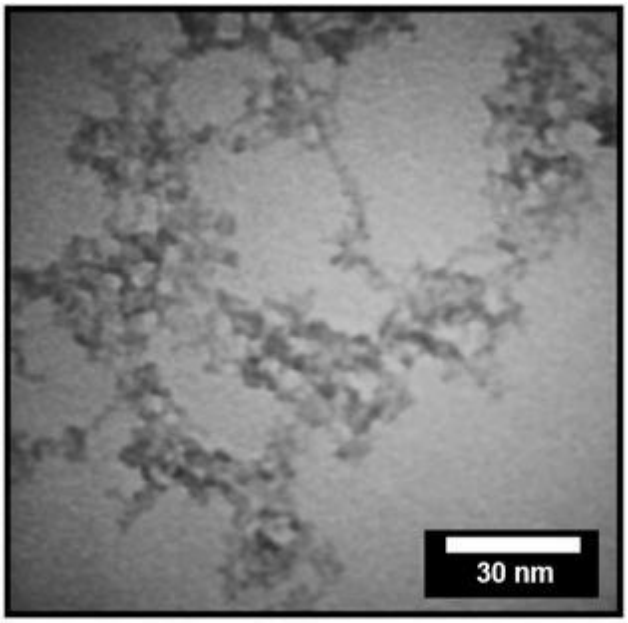

Figure 6. TEM image of TGA- ZnS nanocrystals

The absorption edge (Fig. 7) is found at 3.88 eV and 4.02 eV for ZnS75 and TGA-ZnS, respectively. From the graph, it is clear that in the capped ZnS sample, the absorption peak has blue shifted compared to the uncapped ZnS, which can be attributed to quantum confinement effect. For both capped and uncapped samples, the particle size estimated from Brus equation is 2-4 nm. The optical absorbance properties, crystallite and particle sizes of QDs are compared in Table 3.

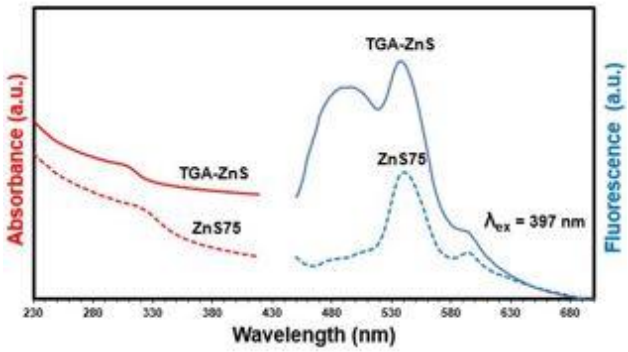

Figure 7. Absorption and PL spectra of ZnS75 and TGA-ZnS QDs

Table 3. Comparison of band edge and mean size of nanocrystals and nanoparticles estimated by various techniques

Sample	Band edge (nm)	Band edge (eV)	Crystallite sizes from EMA (nm)	Particle size (SEM)	Particle size (DLS)
ZnS75	319	3.88	3.63	25-125	52-147
TGA-ZnS	308	4.02	2.74	9-25	8-22

In addition to enhancing colloidal stability, capping agents can improve the luminescent properties of QDs by passivating the surface of nanoparticles resulting in a drop in non-radiative recombination. Room temperature PL spectra of ZnS75 and TGA-ZnS are displayed in Fig. 7. For uncapped QDs, the main emission peaks are found around 538 and 595 nm while for capped ones an extra broad peak centered at 492 nm is observed because of the electronic transitions of interstitial sulfur. The slight variation in the position of the emission peaks can be attributed to the

electronic structure of organic head groups, which affect the energies of trapping levels [65]. The physical processes involved in the PL spectra can be described as follows:

$$ZnS + h\nu \rightarrow ZnS\left(h_{VB}^{+} + e_{CB}^{-}\right) \quad (3)$$

$$I_S + e_{CB}^{-} = I_s^{-} + h\upsilon_1 \quad (4)$$

$$I_s^{-} + h_{VB}^{+} \rightarrow I_s \quad (5)$$

$$I_{Zn} + e_{CB}^{-} \rightarrow I_{Zn}^{-} \quad (6)$$

$$I^{-}_{Zn} + h_{VB}^{+} \rightarrow I_{Zn} + h\upsilon_2 \quad (7)$$

$$V_s + e_{CB}^{-} \rightarrow V_s^{-} \quad (8)$$

$$V_s^{-} + h_{VB}^{+} \rightarrow V_s + h\upsilon_3 \quad (9)$$

$$V_{Zn} + e_{CB}^{-} \rightarrow V_{Zn}^{-} + h\upsilon_4 \quad (10)$$

$$V_{Zn}^{-} + h_{VB}^{+} \rightarrow V_{Zn} \quad (11)$$

Furthermore, it can be seen in Fig. 7 that the emission of nanoparticles becomes more intense in the presence of TGA. This can be ascribed to the surface defect passivation of the nanoparticles, which leads to an increase in the radiative electron-hole recombination. Hence, TGA serves as an efficient capping agent because its thiol groups coordinate easily with Zn^{2+}, which direct to the formation of an organic structure on the surface of QDs, decreasing the surface defects and thus favoring the enhancement of PL intensity.

3.2. MNPs characterization

The XRD pattern of the $CoFe_2O_4$ nanoparticles is reported in Fig. 8a. The positions and relative intensities of the main diffraction peaks at 2θ values of 30.6°, 35.8°, 43.9°, 47.4°, and 62.9° correspond to (220), (311), (400), (510), and (440) lattice lanes prove that the crystalline structure of the products favors the formation of cubic spinel phase (JCPDS NO. 22-1086) without crystalline impurities. The average crystallite size of the as-synthesized nanoparticles is calculated around 8 nm using Scherrer's equation. Besides, a diameter of 30-50 nm for the magnetic particles was determined from DLS measurements (inset of Fig. 8a). The MNPs also show superparamagnetic behavior in VSM analysis with low coercivity and M_s of 40 emu/g (Fig. 8b).

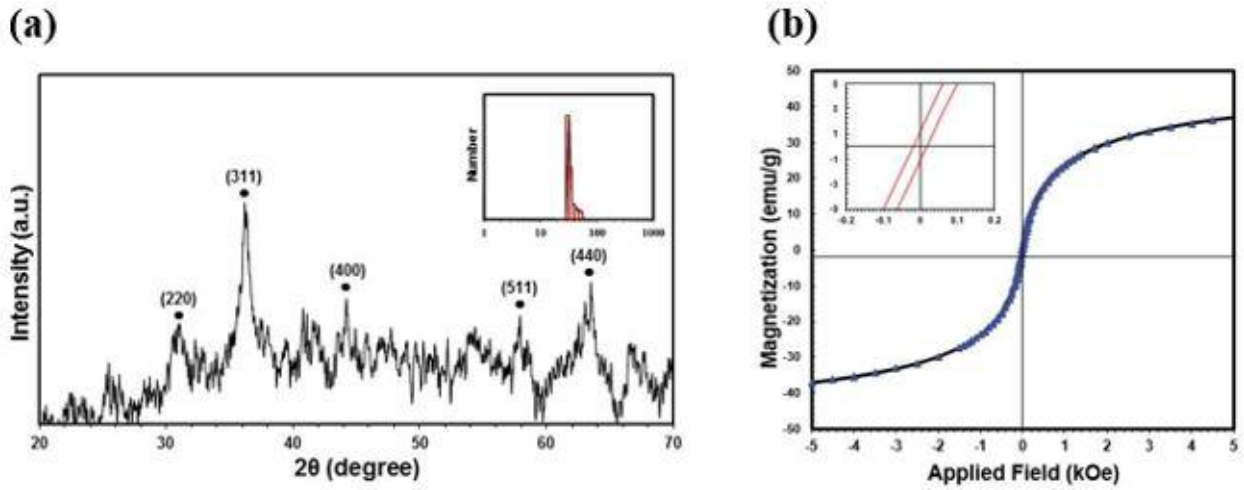

Figure 8. a) XRD pattern and DLS curve (inset) of MNPs. b) Magnetic hysteresis loop of $CoFe_2O_4$ nanoparticles at room temperature

3.3. LMNs characterization

FT-IR spectra of bare, silica coated, functionalized MNPs, and LMNs are shown in Fig. 9a. A characteristic band confirming the presence of magnetic nanoparticles is around 510-600 cm^{-1}, which corresponds to the stretching vibration of Co-O and Fe-O. Also, a broad peak is observed around 2800-3700 cm^{-1} due to the stretching vibration of -OH [44].

In the spectra of silica coated MNPs, the Fe-O-Si absorption band cannot be seen because it appears at 587 cm^{-1}, and overlaps with the Fe-O band. The peaks at 1036 cm^{-1}, 1710 cm^{-1}, and 2800-2900 cm^{-1} are assigned to stretching vibrations of Si-OH, C=O of free carboxylic acid and stretching and bending vibrations of -CH groups [66]. Also, the peaks of 1380-1420 cm^{-1} and 1620 cm^{-1} are consistent with the stretching vibration of the carboxyl groups.

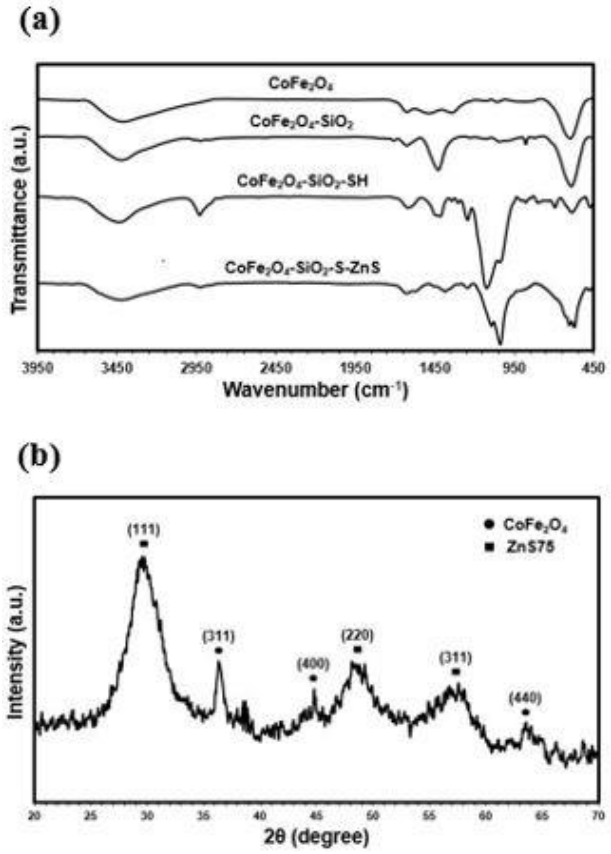

Figure 9. FT-IR spectra (a) and XRD pattern (b) of optomagnetic nanocomposites

As can be seen in the FT-IR spectra of functionalized MNPs, a main peak appears around 1050-1150 cm^{-1} which is attributed to Si-O-Si asymmetric stretch [67]. Finally, the absence of the stretching vibration band of -SH groups at about 2565 cm^{-1} in the spectra of LMNs proves that MPS are attached to ZnS nanoparticles from the thiol end groups. Summarizing, the comparison of characteristic spectral bands illustrates that the surface of $CoFe_2O_4$ is successfully coated with TEOS, functionalized with MPS, and attached to the surface of QDs. Moreover, the XRD pattern of LMNs presents both ZnS and $CoFe_2O_4$ phases, which testifies a successful assembly procedure (Fig. 9b).

Microstructural observations of LMNs are shown in Fig. 10. The particle size of $CoFe_2O_4/SiO_2/ZnS$ is in the range 50–120 nm as evident from the SEM imaging. The TEM image of nanocomposites also illustrates the core-shell nanostructure with a size around 12-45 nm, where the dark particles of MNPs are shielded by a thin layer of bright QDs.

Figure 10c-d shows the EDX mapping images of Co, Fe, Zn, and S of the optomagnetic nonacomposites. It can be seen that the atoms are distributed through the sample and the S atoms have the highest concentration due to the presence of ZnS, TGA, and MPS. Therefore, the ZnS nanoparticles are spread homogeneously all over the nanocomposites.

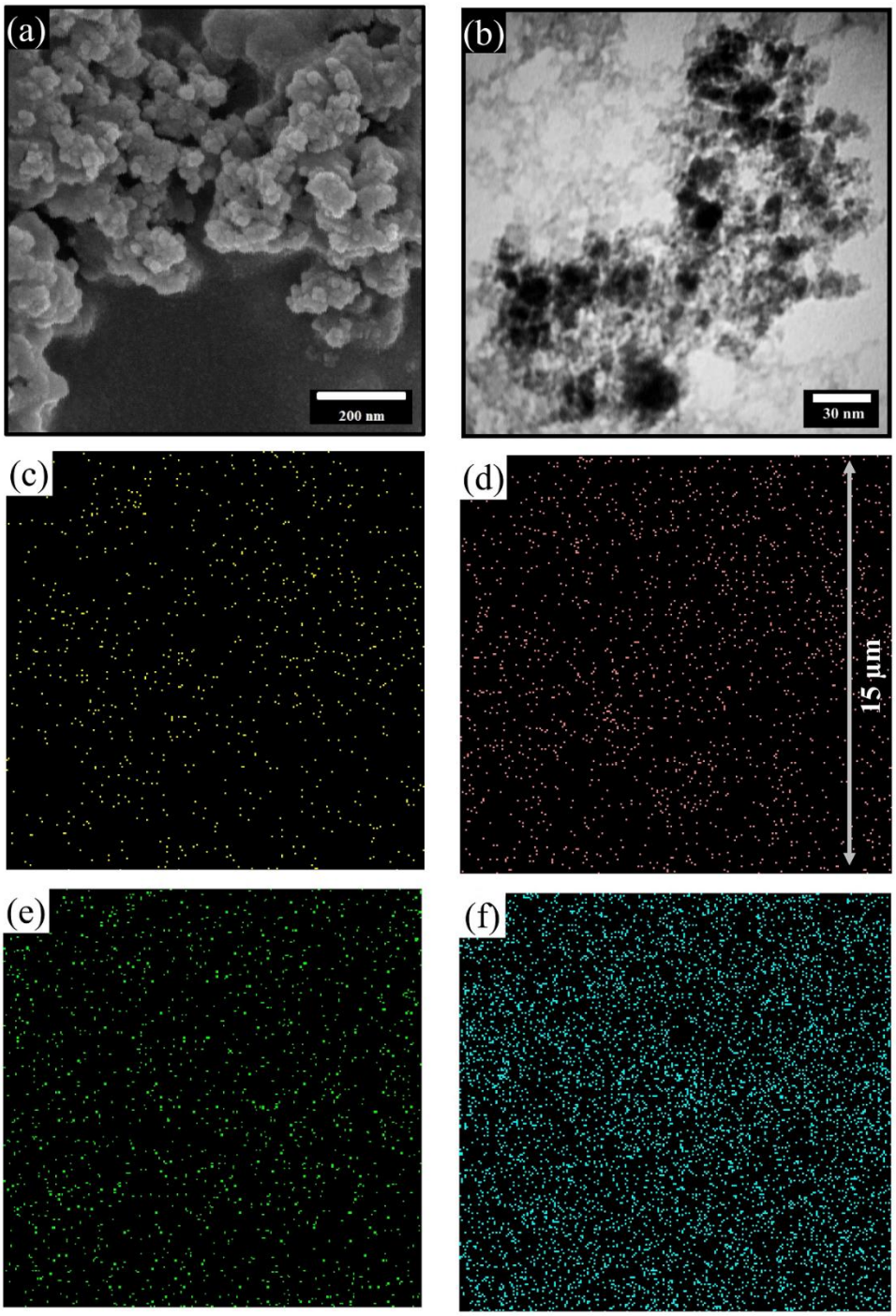

Figure 10. SEM (a) and TEM (b) image of optomagnetic nanocomposites. Element distribution of Co (c), Fe (d), Zn (e), and S (f)

In order to investigate the optical and magnetic properties of LMNs, we synthesized samples with different molar ratio of QDs to MNPs. Figure 11 reveals that although the two main emission peaks in LMNs spectra show no change in position compared with bare QDs, the PL intensity is comparatively reduced. The inset of Fig. 11 depicts that the PL intensity enhances rapidly at low molar ratio and tends to move towards a constant value when the QDs to MNPs ratio comes close to 32:1. The relatively low fluorescence intensity at lower molar ratio is caused by the absorption of MNPs, so-called QDs quenching, because both the light used to excite the QDs and the light emitted from it are strongly absorbed by the MNPs.

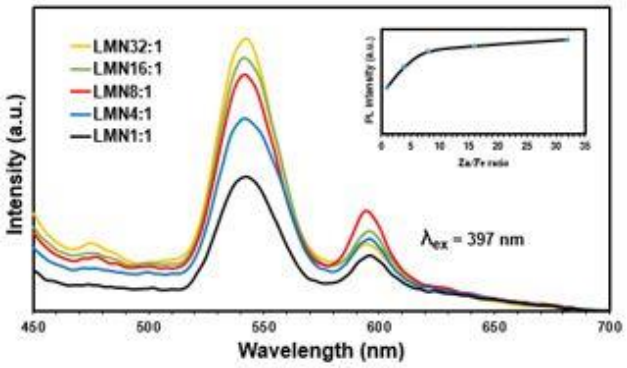

Figure 11. PL spectra and PL intensity (inset) of LMNs at different ratio of QDs to MNPs

Figure 12a shows the hysteresis loop of the LMNs at 298 K. The curve is free from any hysteresis and the coercivity is close to zero which signifies nanoscaled dimension and superparamagnetic behavior of the samples.

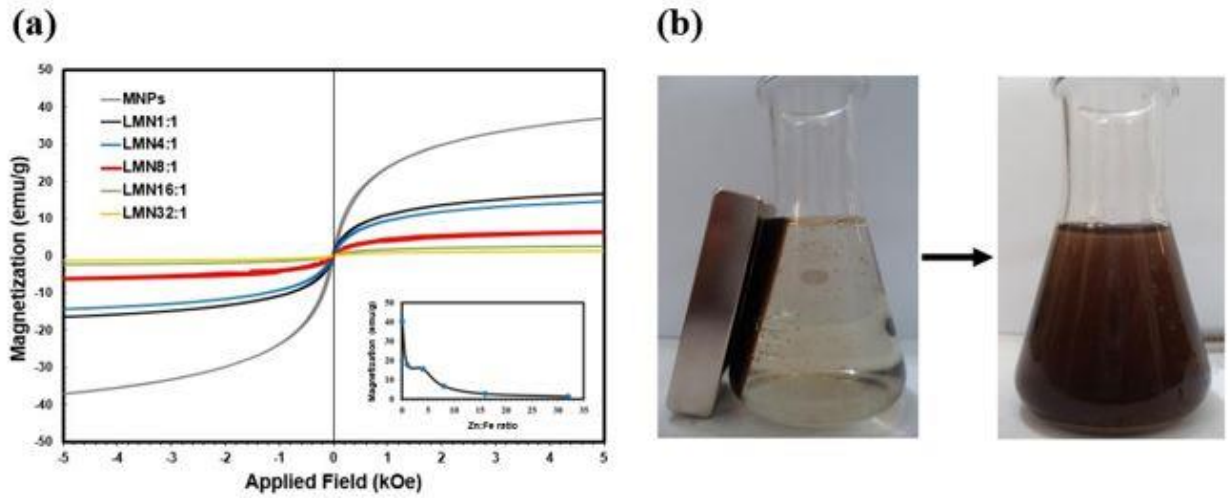

Figure 12. a) Magnetic hysteresis loop and saturation magnetization (inset) of LMNs at different ratio of QDs to MNPs. (b) Dispersion of LMNs in the absence and presence of applied magnetic field

As apparent from Fig. 12a, The M_s of LMN1:1, LMN4:1, LMN8:1, LMN16:1, and LMN32:1 is 17.8, 15.6, 6.7, 2.7, and 1.3 emu/g, respectively. The M_s of all samples is below the value of pure $CoFe_2O_4$. One important factor affecting the M_s is surface weakening of the magnetic moments at the interfaces between the magnetic particles, which occurs at MNPs-silica coating interfaces and causes high effective anisotropy fields and low measured saturation magnetizations [68].

The inset of Fig. 12a illustrates that the M_s decreases with increase in the QDs to MNPs ratio, which can be ascribed to the presence of QDs in optomagnetic nanocomposites. The presence of ZnS might produce anomalous anisotropy or reduced exchange thereby resulting in a lower measured magnetization [69].

Figure 12b demonstrates the harvesting of the LMNs by a magnetic field. In the absence of an external field, the dispersion of the optomagnetic nanocomposite was dark brown and homogeneous. When the external magnetic field was applied, LMNs were enriched, showed

ferrofluidic behavior and the dispersion became clear and transparent. More, after turning off the magnetic field followed by vigorous stirring, the aggregations were quickly redispersed confirming the superparamagnetic behavior of as-synthesized optomagnetic nanocomposites. It is worth noting that if an individual particle had a remanent magnetic property, each particle would react as a small dipole magnet, resulting in particle aggregations. Concisely, as a result of the comprehensive characterizations, LMN8:1 is considered as an optimum sample to yield good quality optomagnetic nanocomposites.

3.5. Conclusions and perspectives

ZnS nanoparticles were successfully synthesized by a wet chemical reaction at different temperatures resulting in crystallite sizes around 2.9-4.3 nm. The observed blue shifts in the optical absorption edges confirmed a quantum confinement effect and the PL emission became more intense and was the highest for the sample prepared at 75 °C. In addition, we reported a progressive method for assembling LMNs with MNPs/SiO_2 core and QDs shell structure. These LMNs had a mean particle size of 12-45 nm and the PL intensity increased rapidly at low ratio of QDs to MNPs and tended to move towards a constant value. We also observed that the M_s decreased with an increase in this ratio because of the presence of ZnS, which leads to a reduction of exchange interactions strength between the neighboring magnetic particles. Consequently, LMN8:1 as an efficient optomagnetic nanocomposite representing a significant step on the way toward a smart multifunctional nanostructure. In a few words, the optical and magnetic properties of these nanocomposites allow them to be used in several applications such as biology and photocatalysts.

Acknowledgements

The authors would like to acknowledge Color & Polymer Research Center (CPRC) for helping us in this project. F.R. is grateful to NSERC for an EWR Steacie Memorial Fellowship.

References

[1] Y. C. Park, J. Paulsen, R. Nap, R. D. Whitaker, V. Mathiyazhagan, Y. Song, M. Hurlimann, I. Szleifer and J. Y. Wong, *Langmuir*, 2014, **30**, 784-792.

[2] A. Cao, R. Lu and G. Veser, Phys. *Chem. Chem. Phys.*, 2010, **12**, 13499-13510.

[3] S. Anas, K. V. Mahesh, V. Jobin, S. Prasanth and S. Ananthakumar, *J. Mater. Chem. C*, 2013, **1**, 6455-6462.

[4] G. Boulon, G. Alombert-Goget, Y. Guyot, M. Guzik, T. Epicier, N. P. Blanchard, L. Chen, L. Hu and W. Chen, *J. Mater. Chem. C*, 2014, **2**, 9385-9397.

[5] P. Zhou, H. Wei, Q. Sun, P. Wang, S. Ding, A. Jiang and D. W. Zhang, *J. Mater. Chem. C*, 2013, **1**, 2548-2552.

[6] Y. Fang, J. Hou and Y. Fang, *J. Mater. Chem. C*, 2014, **2**, 1178-1183.

[7] A. Saha, SK. Basiruddin, N. Pradhan and N. R. Jana, *Langmuir*, 2009, **26**, 4351-4356.

[8] K. K. Senapati, C. Borgohain and P. Phukan, *Cata. Sci. Technol*. 2012, **2**, 2361-2366.

[9] N. Chekina, D. Horák, P. Jendelová, M. Trchová, M. J. Beneš, M. Hrubý, V. Herynek, K. Turnovcová and E. Syková, *J. Mater. Chem.*, 2011, **21**, 7630-7639.

[10] H. M. Fan, M. Olivo, B. Shuter, J. B. Yi, R. Bhuvaneswari, H. R. Tan, G. H. Xing, C. T. Ng, L. Liu, L. L. Lucky, B. H. Bay and J. Ding, *J. Am. Chem. Soc*., 2010, **132**, 14803-14811.

[11] C. Y. Ang, L. Giam, Z. M. Chan, A. W. H. Lin, H. Gu, E. Devlin, G. C. Papaefthymiou, S. T. Selvan and J. Y. Ying, *Adv. Mater.,* 2009, **21**, 869-873.

[12] F. Zhan and C. Zhang, *J. Mater. Chem.*, 2011, **21**, 4765-4767.

[13] X. You, R. He, F. Gao, J. Shao, B. Pan and D. Cui, *Nanotechnology*, 2007, **18**, 035701.

[14] H. He, M. Y. Xie, Y. Ding and X. F. Yu, *Appl. Surf. Sci.*, 2009, **255**, 4623-4626.

[15] J. M. Shen, L. Xu, Y. Lu, H. M. Cao, Z. G. Xu, T. Chen and H. X. Zhang, *Int. J. Pharm.*, 2012, **427**, 400-409.

[16] X. Liu, Z. Fang, X. Zhang, W. Zhang, X. Wei and B. Geng, *Cryst. Growth Des*., 2008, **9**, 197-202.

[17] Q. Xiao and C. Xiao, *Nanoscale Res. Lett.*, 2009, **4**, 1078-1084.

[18] H. Lu, G. Yi, S. Zhao, D. Chen, L. H. Guo and J. Cheng, *J. Mater. Chem*., 2004, **14**, 1336-1341.

[19] X. Yu, J. Wan, Y. Shan, K. Chen and X. Han, *Chem. Mater.,* 2009, **21**, 4892-4898.

[20] A. Luque, A. Marti, A. Mellor, D. F. Marron, I. Tobias and E. Antolin, *Prog, Photovoltaics: Res. Appl.*, 2013, **21**, 658-667.

[21] K. Katsiev, A. H. Ip, A. Fischer, I. Tanabe, X. Zhang, A. R. Kirmani, O. Voznyy, L. R. Rollny, K. W. Chou, S. M. Thon, G. H. Carey, X. Cui, A. Amassian, P. Dowben and E. H. Sargent, *Adv. Mater*., 2014, **26**, 822-822.

[22] S. Moosakhani, A. A. Sabbagh Alvani, A. A. Sarabi, H. Sameie, R. Salimi, S. Kiani and Y. Ebrahimi, *Mater. Res. Bull.*, 2014, **60**, 38-45.

[23] E. Mohagheghpour, F. Moztarzadeh, M. Rabiee, M. Tahriri, M. Ashuri, H. Sameie, R. Salimi and S. Moghadas, *IEEE Trans Nanobioscience*, 2012, **11**, 317-323.

[24] B. Chon, S. L. Lim, W. Kim, J. Seo, H. Kang, T. Joo, J. Hwang and S. K. Shin, *Phy. Chem. Chem. Phys*., 2010, **12**, 9312-9319.

[25] T. Endres, M. Zheng, A. Kiliç, A. Turowska, M. B. Broichsitter, H. Renz, O. M. Merkel and Kissel, T. Amphiphilic Biodegradable PEG-PCL-PEI Triblock Copolymers for FRET-Capable in Vitro and in Vivo Delivery of siRNA and Quantum Dots. *Mol. Pharmaceutics* **2014**, 11, 1273-1281.

[26] W. Moreels, K. Lambert, D. D. Muynck, F. Vanhaecke, D. Poelman, J. C. Martins, J. Allan and Z. Hens, *Chem. Mater.*, 2007, **19**, 6101-6106.

[27] G. Murugadoss and V. Ramasamy, *Luminescence,* 2013, **28**, 195-201.

[28] S. Santra, H. Yang, P. H. Holloway, J. T. Stanley and R. A. Mericle, *J. Am. Chem. Soc*., 2005, **127**, 1656-1657.

[29] C. Finetti, M. Colombo, D. Prosperi, G. Alessio, C. Morasso, L. Sola and M. Chiari, *Chem. Commun*., 2014, **50**, 240-242.

[30] H. Labiadh, T. B. Chaabane, L. Balan, N. Becheik, S. Corbel, G. Medjahdi and R. Schneider, *Appl. Catal. B-Environ*., 2014, **144**, 29-35.

[31] X. Wang, J. Shi, Z. Feng, M. Li and C. Li, *Phys. Chem. Chem. Phy.*, 2011, **13**, 4715-4723.

[32] Z. Zhang, J. She, H. Chen, S. Deng and N. Xu, *J. Mater. Chem. C,* 2013, **1**, 4970-4978

[33] S. F. Wuister and A. Meijerink, *J. lumin*. 2003, **102**, 338-343.

[34] H. Qian, C. Dong, J. Weng and J. Ren, *Small*, 2006, **2**, 747-751.

[35] J. Liu, Z. Shi, Y. Yu, R. Yang and S. Zuo, *J. Colloid Interf. Sci.*, 2010, **342**, 278-282.

[36] X. Xue, Y. Huang, Z. Zhuang, F. Huang and Z. Lin, *CrystEngComm.*, 2013, **15**, 4963-4969.

[37] S. Gao, X. Wu, H. Jiang, D. Chen, O. Li, X. Liu and X. Wang, *RSC Adv.*, 2014, **4**, 20841-20846.

[38] J. Livingston and C. Bean, *J. Appl. Phys*., 2009, **30**, 318-319.

[39] Q. Cao, Z. Liu and R. Che, *New J. Chem*., 2014, **38**, 3193-3198.

[40] D. Bahadur, J. Giri, B. B. Nayak, T. Sriharsha, P. Pradhan, N. K. Prasad, K. C. Barick and R. D. Ambashta, *Pramana,* 2005, **65**, 663-679.

[41] Y. I. Kim, D. Kim and C. S. Lee, *Physica B*, 2003, **337**, 42-51.

[42] M. Liu, L. Xu, W. Cheng, Y. Zeng and Z. Yan, *Spectrochim. Acta A*, 2008, **70**, 1198-1202.

[43] K. Maaz, A. Mumtaz, S. K. Hasanain and A. Ceylan, *J. Magn. Magn. Mater.*, 2007, **308**, 289-295.

[44] M. Sangmanee and S. Maensiri, *Appl. Phys. A*, 2009, **97**, 167-177.

[45] S. Lian, E. Wang, Z. Kang, Y. Bai, L. Gao, M. Jiang, C. Hu and L. Xu, *Solid State Commun.*, 2004, **129**, 485-490.

[46] S. Zhou, Q. Chen, X. Hu and T. Zhao, *J. Mater. Chem*., 2012, **22**, 8263-8270.

[47] G. H. Du, Z. L. Liu, X. Xia, Q. Chu and S. M. Zhang, *J. sol-gel sci. tech.*, 2006, **39**, 285-291.

[48] S. T. Selvan, T. T. Y. Tan, D. K. Yi and N. R. Jana, *Langmuir*, 2009, **26**, 11631-11641.

[49] Y. Zhang, S. N. Wang, X. D. Zhang, S. Ma, Z. D. Zhang, J. J. Guan and D. Li, *J. Biomed. Mater. Res. A,* 2008, **85**, 840-846.

[50] Y. Ebrahimi, A. A. Sabbagh Alvani, A. A. Sarabi, H. Sameie, R. Salimi, M. Sabbagh Alvani and S. Moosakhani, *Ceram. Int.*, 2012, **38**, 3885-3892.

[51] Y. Yin and A. P. Alivisatos, *Nature*, 2004, **437**, 664-670.

[52] R. Salimi, H. Sameie, A. A. Sabbagh Alvani, F. Nargesian, A. A. Sarabi, A. A. Sabbagh Alvani, H. Eivaz Mohammadloo and M. Tahriri, *J. Opt. Soc. Am. B*, 2013, **30**, 1747-1754.

[53] Y. Xiaodan, W. Qingyin, J. Shicheng and G. Yihang, *Mater. Charact.*, 2006, **57**, 333-341.

[54] O. I. Micic, C. J. Curtis, K. M. Jones, J. R. Sprague and A. J. Nozik, *J. Phys. Chem.*, 1994, **98**, 4966-4969.

[55] D. Mitra, I. Chakraborty and S. P. Moulik, *Colloid J.*, 2005, **67**, 445-450.

[56] M. Kanemoto, H. Hosokawa, Y. Wada, K. Murakoshi, S. Yanagida, T. Sakata, H. Mori, M. Ishikawa and H. Kobayashi. *J. Chem. Soc.*, 1996, **92**, 2401-2411.

[57] Y. Li, Y. Ding, Y. Zhang and Y. Qian, *J. Phys. Chem. Solids*, 1999, **60**, 13-15.

[58] M. Taherian, A. A. Sabbagh Alvani, M. A. Shokrgozar, R. Salimi, S. Moosakhani, H. Sameie and F. Tabatabaee, *Elec. Mater. Lett.*, 2014, **10**, 393-400.

[59] S. K. Mehta, S. Kumar, S. Chaudhary, K. K. Bhasin and M. Gradzielski, *Nanoscale Res. Lett.*, 2009, **4**, 17-28.

[60] S. Lee, D. Song, D. Kim, J. Lee, S. Kim, I. Y. Park and Y. D. Choi, *Mater. Lett.*, 2004, **58**, 342-346.

[61] A. A. Khosravi, M. Kundu, L. Jatwa, S. K. Deshpande, U. A. Bhagwat, M. Sastry and S. K. Kulkarni, *Appl. Phys. Lett.*, 1995, **67**, 2702-2704.

[62] R. N. Bhargava, D. Gallagher, X. Hong and A. Nurmikko, *Phys. Rev. Lett.*, 1994, **72**, 416-419.

[63] R. Xie, Y. Li, L. Liu, L. Yang, D. Xiao and J. Zhu, *Mater. Charact*., 2011, **62**, 582-587.

[64] M. Sharma, S. Kumar and O. Pandey, *J. Nanopart. Res.*, 2010, **12**, 2655-2666.

[65] S. Mehta, S. Kumar and M. Gradzielski, *J. Colloid Interf. Sci.*, 2011, **360**, 497-507.

[66] M. H. Mashhadizadeh and M. Amoli-Diva, *J. Anal. At. Spectrom*., 2013, **28**, 251-258.

[67] L. L. Rouhana and J. B. Schlenoff, *J. Nanopart. Res.*, 2012, **14**, 1-11.

[68] R. Kas, E. Sevinc, U. Topal and H. Y. Acar, *J. Phys. Chem. C*, 2010, **114**, 7758-7766.

[69] A. E. Berkowitz, J. A. Lahut, I. S. Jacobs, L. M. Levinson and D. W. Forester, *Phys. Rev. Lett.* 1975, **34**, 594-597.